

Composites Part A: Applied Science and Manufacturing 156 (2022), 106858

<https://doi.org/10.1016/j.compositesa.2022.106858>

Accepted 1 February 2022

Advancements in carbon fibre reinforced ultra-refractory ceramic composites: effect of rare earth oxides addition

Antonio Vinci*

CNR-ISTEC, Institute of Science and Technology for Ceramics, Via Granarolo 64, I-48018 Faenza, Italy

antonio.vinci@istec.cnr.it

Laura Silvestroni

CNR-ISTEC, Institute of Science and Technology for Ceramics, Via Granarolo 64, I-48018 Faenza, Italy

laura.silvestroni@istec.cnr.it

Nicola Gilli

CNR-ISTEC, Institute of Science and Technology for Ceramics, Via Granarolo 64, I-48018 Faenza, Italy

nicola.gilli@istec.cnr.it

Luca Zoli

CNR-ISTEC, Institute of Science and Technology for Ceramics, Via Granarolo 64, I-48018 Faenza, Italy

luca.zoli@istec.cnr.it

Diletta Sciti

CNR-ISTEC, Institute of Science and Technology for Ceramics, Via Granarolo 64, I-48018 Faenza, Italy

diletta.sciti@istec.cnr.it

* Corresponding author. Tel: +39 546699723. E-mail: antonio.vinci@istec.cnr.it (Antonio Vinci)

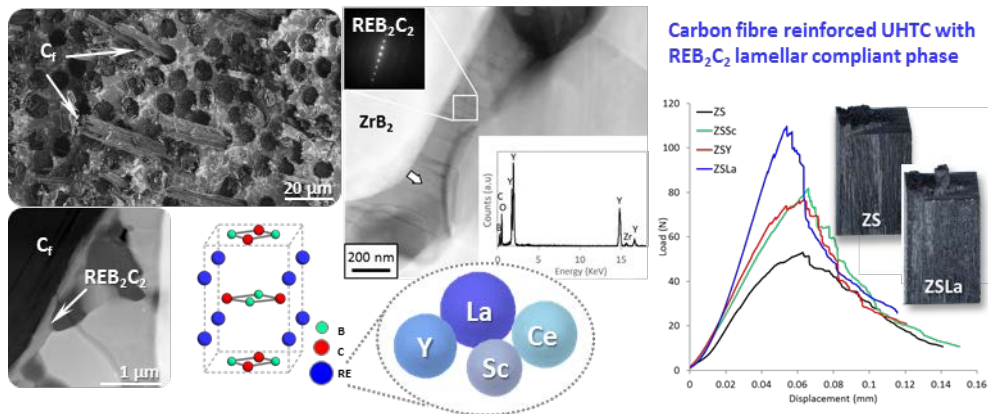
Abstract

Continuous carbon fibre ceramic matrix composites capable of tolerating multiple thermal-shock cycles and resisting ablation are needed for aerospace and hypersonic systems. Carbon fibre around 50 vol% and ultra-refractory matrices are fundamental parameters. The influence of rare earth (RE) oxides on the microstructure and mechanical properties of carbon fibre-ZrB₂/SiC composites was investigated. Materials were produced by slurry infiltration and hot pressing. The addition of Y₂O₃, La₂O₃ and CeO₂ led to the formation of lamellar boro-carbides that improved the densification, while Sc₂O₃ promoted the formation of (Zr,Sc)B₂ solid solutions in the matrix. All these composites exhibited improved mechanical properties compared to a RE-free baseline, with room temperature strengths and toughness above 330 MPa and 9 MPa·m^{0.5}, respectively, and strengths above 600 MPa at 1500°C. The lamellar phase was identified as a fibre by-product with general formula REB₂C₂. Only CeO₂ was detrimental on the long run due to its high reactivity with humidity which induced swelling and jeopardized the structural stability of the composite.

This study revealed new fundamental insights into the microstructure evolution of carbon-fibre refractory composites and its impact on the mechanical properties, which will contribute to the development of new generation of reusable ceramic matrix composites for harsh environments.

Keywords: Carbon fibre, Ceramic-Matrix Composites (CMCs); Rare Earth oxides; Microstructure; Mechanical properties.

Graphical abstract



1. Introduction

The growing demand for materials able to withstand the extremely hot environments of aerospace and propulsion and the increasingly more challenging requirements concerning the resistance and reusability of these materials has led to the development of a new class of ceramic matrix composites based on an ultra-high temperature ceramic (UHTC) matrix reinforced with carbon fibres (Cf). The

conventional materials, based on Cf/SiC or Cf/C ceramic matrix composites (CMCs), can no longer satisfy the current requirements of oxidation resistance above 2000°C and reusability,[1] while other refractory bulk ceramics, such as UHTCs, could possess excellent ablation resistance, but are too susceptible to thermal shocks and cracking.[2] The idea of combining these two classes of materials led to the integration of a UHTC matrix in CMCs, allowing to retain the high ablation resistance of the former, and the damage tolerance provided by the fibre reinforcement. The preferred UHTC matrix is typically based on ZrB₂ because of its relatively low density [3], high thermal conductivity [4], lower cost compared to Hf-based ceramics and good oxidation resistance when doped with SiC [5][6][7]. In the last decade, several studies have been carried out on this new class of materials labelled UHTCMCs and many approaches have been employed to combine the fibre reinforcement with the UHTC matrix [8][9][10]. One approach is based on the dispersion of UHTC particles in the carbon or SiC matrix of conventional CMCs in order to increase their ablation resistance. Another approach consists in reinforcing a UHTC matrix with either short or long fibres [11][12][13][14]. This second approach can be more challenging as it requires the homogeneous dispersion of the fibres and a sintering step in order to consolidate the matrix [15], but it is also the most promising in terms of final properties. Previous studies on the mechanical properties and the oxidation behaviour of these materials have shown that these composites have strengths in the range of 300 – 500 MPa and fracture toughness in the order of 6 – 10 MPa·m^{0.5} [16][17][18][19], while oxy-acetylene torch tests and arc-jet wind tunnel tests have demonstrated the materials ability to survive extreme environments, thanks to the formation of a protective zirconia/silica scale [20][21][22][23]. Even though these preliminary results are very promising, there is still room for improvement when it comes to the fabrication and consolidation of these composites. In previous studies, the influence of sintering parameters on the densification of ZrB₂/SiC based UHTCMCs was investigated and found out that higher temperatures would lead to a better densification but also degrade the fibres, and therefore a compromise had to be reached in order to preserve the fibres integrity [24][25][26]. The addition of specific additives could promote densification of the material without damaging the fibres, and in this regard rare earth oxides (REOs) have been reported to aid the sintering of ZrB₂-based ceramics thanks to the formation of a low melting oxide mixture [27]. Our most recent work on the oxidation resistance of a C-ZrB₂/SiC/Y₂O₃ composite has shown the ability of Y₂O₃ to aid the sintering of Cf-ZrB₂/SiC composites and improve the mechanical properties, but also showed how the presence of carbon in the system led to additional reactions that resulted in the formation of new secondary phases containing Y, B and C [28]. Although it was hypothesized that the phase formed was yttrium borocarbide, no conclusive evidence was provided, and neither its role in the densification was assessed.

Rare earth boro-carbides, with generic formula REB_2C_2 ($RE =$ rare earth metal) are layered compounds where the RE metal cations are intercalated within the planar BC rings. The main example reported in literature is YB_2C_2 , of which two crystal structures, $P4_2/mmc$ and $P4/mbm$, have been identified: in the former, boron and carbon are coupled together, in the latter boron and carbon alternate in the B_2C_2 rings (Fig. 1) [29][30][31][32].

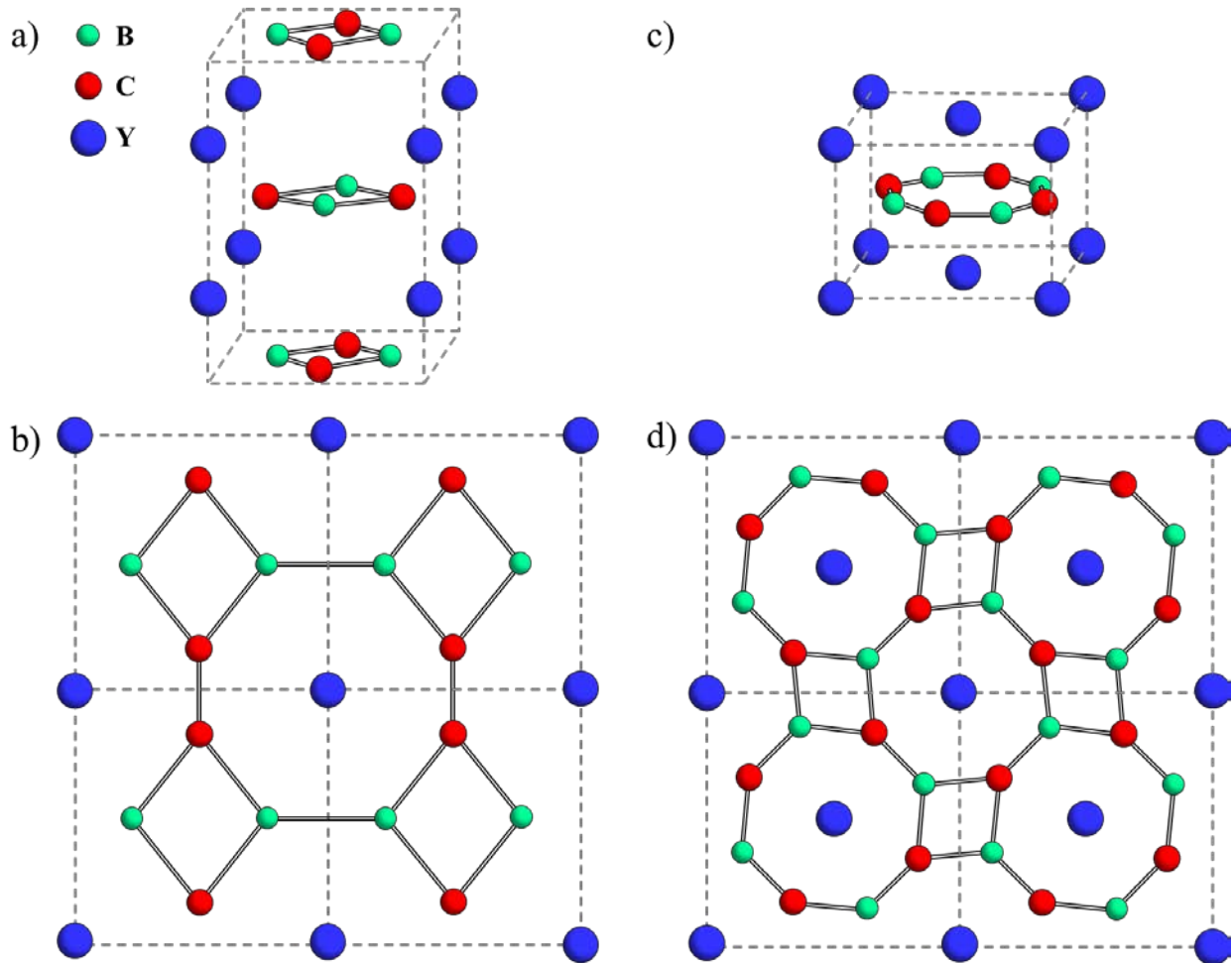


Figure 1. Crystal structure of YB_2C_2 : a) crystal structure of $P4_2/mmc$ YB_2C_2 , b) supercell $2 \times 2 \times 1$ of $P4_2/mmc$ YB_2C_2 , c) crystal structure of $P4/mbm$ YB_2C_2 , d) supercell $2 \times 2 \times 1$ of $P4/mbm$ YB_2C_2 .

They are mostly of interest in the field of superconductors because of their interesting electronic and magnetic properties, but their lamellar structure and refractory nature could be exploited in the field of ceramic composites to obtain unique properties [33]. They are principally produced by reacting elemental boron and carbon with the corresponding metal, but other synthesis routes have been reported involving the use of carbon, a boron source (eg, B_4C or BN), and a REO [34]. In our case, the carbon source would be the fibre reinforcement, the boron source would be the B_2O_3 present on the surface of ZrB_2 particles, and the RE would come from the REO used as additive. In view of the significantly improved mechanical properties reported in the same work, it is likely that these lamellar phases found at the fibre/matrix interface or between ZrB_2 grains further contribute to the toughening

of the composite. Sc, La and Ce have been reported to form the corresponding boro-carbides, but they have never been considered before for their properties as structural materials [32][35][36].

In the present paper, we explored the effect of the addition of group IIIb REOs on the microstructure assembly and resulting mechanical properties of Cf-ZrB₂/SiC composites. The composites were doped with 5 vol% of the various RE oxide (Sc₂O₃, La₂O₃, CeO₂) and compared to a REO-free baseline composite containing only SiC and the previously studied Y₂O₃-doped material.

2. Experimental

2.1. Materials and processing

The composites were produced by slurry infiltration of unidirectional carbon fibre preforms with ceramic powder aqueous suspensions, followed by hot pressing at 1900°C. Fibre layers were laid up in a 0/0° configuration. The details pertaining the process and sintering behaviour of these composites have been reported in previous papers [15]. The raw materials used for the fabrication of these composites are listed below:

ZrB₂ (H.C. Starck, grade B, size 1.5 – 3 μm, Hf < 0.2%), α-SiC 25 UF (H.C. Starck, grade UF-25, size 0.45 μm), Sc₂O₃ (Auer-remy GmbH, 99.9%), Y₂O₃ (H.C. Starck, 99.5% grade C, size 0.90 μm), La₂O₃ (Merck, 99.9%), CeO₂ (Merck, 99.9%, size < 5 μm), and Carbon fibre XN80 (Granoc, Yarn XN80-6k, E=780 GPa, σ_{tens.} = 3.4 GPa, Ø = 10 μm). The baseline matrix, ZS, contained 95 vol% ZrB₂ + 5 vol% SiC. The ceramic matrix compositions of the REO-doped specimens consisted of ZrB₂ + 5 vol% SiC + 5 vol% REO (REO = Sc₂O₃, Y₂O₃, La₂O₃, CeO₂) and were labelled ZSSc, ZSY, ZSLa and ZSCe, respectively.

2.2. Microstructure analysis

The microstructure and phase composition of the polished and fractured surfaces was analysed by field emission scanning electron microscopy (FE-SEM, Carl Zeiss Sigma NTS GmbH Oberkochen, Germany) coupled with an energy dispersive x-ray spectroscopy probe (EDS, INCA Energy 300, Oxford instruments, UK). The specimens were cut from the sintered pellets using diamond blades and were polished down to a 0.25 μm finish with a semi-automatic polishing machine (Tegramin-25, Struers, Italy). The polished samples were cleaned with ethanol and dried under IR light. Finally, the specimens were cleaned with a plasma cleaner (Colibrì Plasma RF 50 KHz, Gambetti, Italy) at 50 W for 3 min.

Specimen fragments of sintered pellets were ground by hand and passed through a 325 μm sieve for X-ray diffraction analysis which was carried out with a Bruker D8 Advance apparatus (Bruker, Karlsruhe, Germany).

TEM specimen from a selected sintered ceramic was prepared by cutting a 3 mm wide disc from the bulk material and mechanically ground down to about 80 μm . Then, a 60 μm deep bowl was created in the center of the disc using a dimpler equipped with a diamond covered wheel leaving the sample at a thickness of 20 μm in the center. The final thinning was performed with an argon ion beam until incipient perforation occurred. Additionally, other TEM samples were prepared by grinding a portion of the sintered materials into a fine powder using an agate mortar. The powder obtained was suspended in isopropyl alcohol and sonicated until homogeneously dispersed. A few drops of this suspension were then dropped onto a Cu grid coated with an ultra-fine carbon film. Electron diffraction peaks were resolved through the commercial software JEMS (Java Electron Microscopy Software, P. Stadelmann, Switzerland).

The fibre and ceramic phases volumetric contents were measured by image analysis using software Image-Pro Analyser 7.0, following the guidelines of standard ISO 13383-1, method A2. At least 3 images per sample were used. The fibre volume and experimental density were used to calculate the matrix volume fraction, x_m , from the equation 1:

$$\rho_{exp} = x_m \rho_m + x_f \rho_f \quad (1)$$

Since the fibre volume fraction was measured on the whole composite, and the total area of interest included the matrix and porosity volume fractions, the porosity, x_p , was calculated from equation 2:

$$1 = x_m + x_f + x_p \quad (2)$$

For specimens ZS and ZSY, already studied in our previous works, the matrix composition contents have been readjusted following these new equations.

2.3. Mechanical testing

Specimens of size 2.0 mm \times 2.5 mm \times 25 mm (thickness \times width \times length) were cut from the sintered pellets along the fibre length. This 0/0° configuration was chosen to minimise data scatter deriving from the different layer sequence of 0/90° specimens after machining of samples previously studied in our earlier works [37][38].

The room temperature flexural strength was measured with a universal testing machine (Zwick Roell Z050 GmbH & Co, KF, Ulm-Eisingen, Germany) using a fully-articulated 4-point steel fixture with a lower span of 20 mm, an upper span of 10 mm and a crosshead speed of 1 mm min^{-1} , following the guidelines of standard ISO/DIS 14704.

The high temperature flexural strength at 1500 °C was measured following the standard of advanced technical ceramics EN 843-1:2006 with a screw-driven testing machine (1195, INSTRON, USA) using a semi-articulated alumina 4-point fixture with a lower span of 20 mm and an upper span of 10 mm and at a cross-head and heated up to 1500°C with a rate of 10°C/min under a constant flow

of argon (3.5 L/min) in a high temperature furnace (HTTF model 924, Severn Furnaces Limited, UK). Specimens were held at 1500°C for 15 min before testing, rate of 1 mm/min were used.

The fracture toughness (K_{Ic}) was evaluated by fracturing chevron notched beams (CNB), following the guidelines of EN 14425-3 (2010). The test bars, 2.5 mm × 2.0 mm × 25 mm (thickness × width × length), were notched with a 0.1 mm-thick diamond saw; the chevron-notch tip depth and average side length were ~0.12 and ~0.80 of the bar thickness, respectively. The same machine employed for the room temperature flexural strength was used. At least 3 specimens per test were used for each property.

3. Results and discussion

3.1 X-Ray diffraction analysis

XRD analysis performed on the cross-section of the sintered specimens (Fig. 2) showed that the main peaks were ZrB₂ (PDF#75-1050) with trace amounts of ZrC (PDF#74-1221), and α-SiC (PDF#29-1131). Some new peaks were detected at high 2-theta angles, and potentially belonging to RE-based second phases, like YB₂C₂ (PDF#65-2830) or LaB₂C₂ (PDF#26-0811), but their intensity was too low to ultimately define their nature. For the ZSSc sample, a shift on the right and broadening of ZrB₂ peaks was observed, especially at high 2θ-angles, which could be attributed to the formation of a (Zr,Sc)B₂ solid solution with shorter lattice, since Sc and Zr have very close atomic radii 161 pm and 160 pm, respectively, and ScB₂ signals fall in the same region (PDF#32-0988).

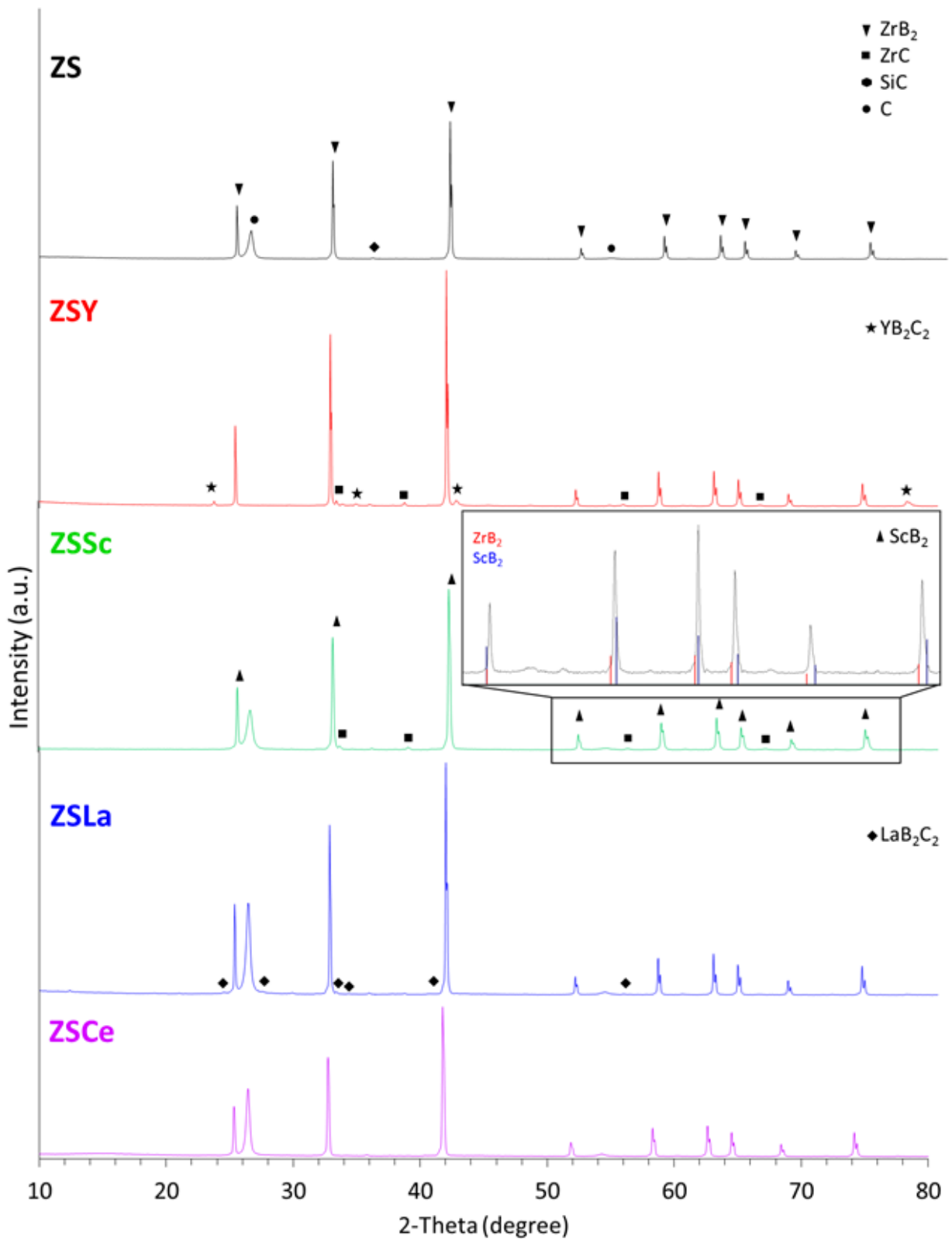


Figure 2. X-ray diffraction pattern of the sintered specimens. In all samples the main phase detected was ZrB_2 (PDF#75-1050) with trace amounts of ZrC (PDF#74-1221) and $\alpha\text{-SiC}$ (PDF#29-1131). The inset in ZSSc sample evidences ZrB_2 peak shift on the right and broadening suggesting formation of a $(\text{Zr,Sc})\text{B}_2$ solid solution.

3.2 Microstructure of the sintered composites

The physical properties and phase volumetric contents in the sintered composites are reported in Table 1. The data relative to sample ZS and ZSY were taken from our previous work for comparison purposes [28]. Slight variations (~3 vol%) in the fibre contents were attributed to the variability of the manual process, but in the case of sample ZSCe, infiltration was particularly more challenging and resulted in a lower fibre amount compared to other samples, 38 vol% vs 48-50 vol%. In order to account for the formation of new phases in the calculation of the theoretical density, ρ_{theor} , phases volumetric contents were measured by image analysis and normalized on the whole composite. The proportions between ZrB_2 and SiC remained constant in all specimens after sintering, suggesting that SiC did not undergo any significant reaction. However, for sample ZSY, a considerably lower SiC content was found, around 1 vol% vs the initial 3 vol%, indicating that a reaction involving SiC took place in this case. On the contrary, no pure REO was found for any compositions, but a new RE-B-C phase was found at its place. The volumetric amounts of the RE-B-C phases were comparable with the nominal values relative to the corresponding oxides. In all cases, the addition of the RE-oxides led to porosity decrease, with Y_2O_3 being the most effective sintering aid.

Table 1. Phases volumetric amounts as measured by image analysis and density values for samples ZS, ZSY, ZSSc, ZSLa and ZSCe.

Sample	Composition (vol%)						ρ_{theor} (g/cm ³)	$\rho_{\text{exp.}}$ (g/cm ³)	$\rho_{\text{rel.}}$ (g/cm ³)	Ref.
	ZrB ₂	SiC	ZrC	REB ₂ C ₂	Fibre	Porosity				
ZS	43.5	2.6	0.1	-	47.9	5.9	3.97	3.74	94.1	[28]
ZSSc	44.1	2.4	1.1	-	46.7	5.7	4.08	3.85	94.3	-
ZSY	44.9	1.1	0.3	2.5	50.3	0.9	4.03	3.99	99.0	[28]
ZSLa	39.3	2.7	-	2.3	50.9	4.8	3.86	3.68	95.2	-
ZSCe	51.0	3.1	-	3.6	38.1	4.2	4.36	4.18	95.8	-

Sample ZS and ZSY have been already covered in our previous work [28], but their microstructural features is here reported for convenience of comparison.

Sample **ZS** was characterized by a homogeneous distribution of fibres and SiC particles in the ZrB_2 matrix, Fig. 3. Porosity was mainly found at ZrB_2 grain junctions and no grain growth was observed after sintering.

In all cases, fibres were well anchored to the matrix and some ZrC was found at the fibre/matrix interface, deriving from the reduction of the ZrO₂, present on the surface of ZrB₂ particles, with the carbon of the fibre. No other phases were detected by EDS.

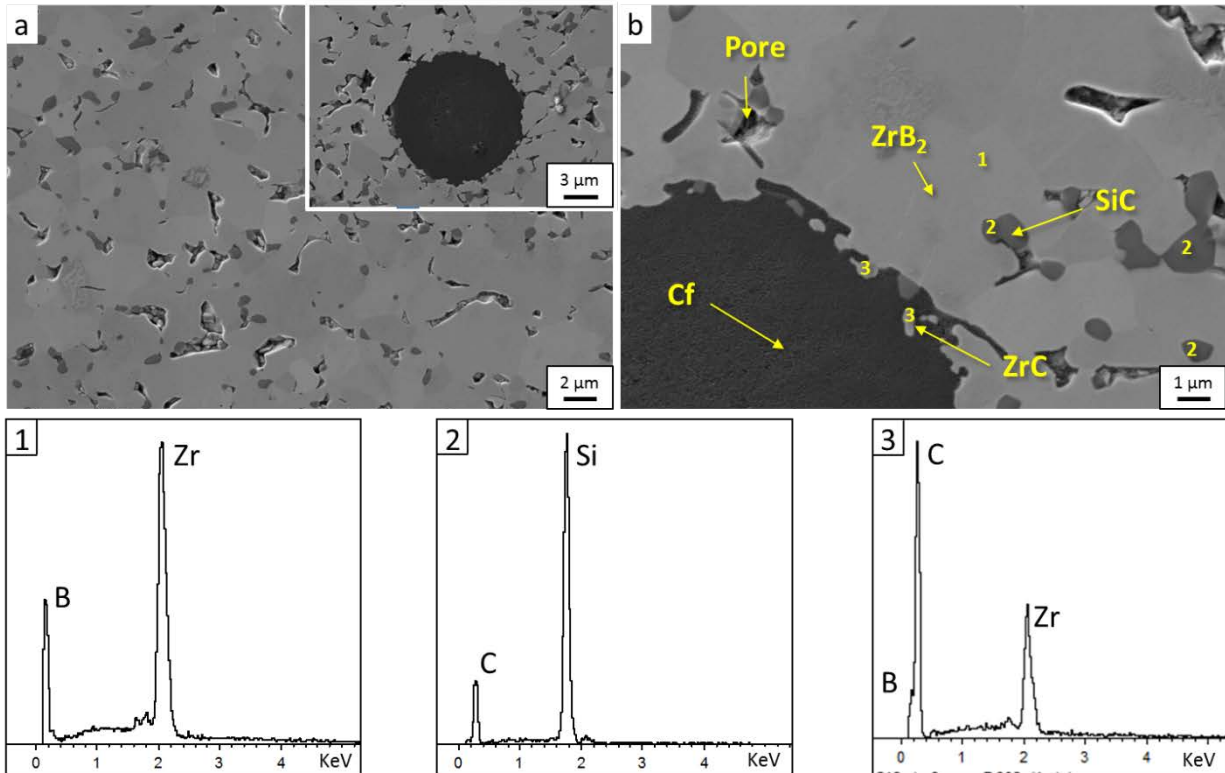


Figure 3. Microstructure of sample ZS: a) microstructure of the ceramic matrix showing porosity and inset of the fibre cross section, b) detail of the fibre/matrix interface with corresponding EDS spectra.

For the **ZSSc** sample, the majority of Sc was found as a (Zr,Sc)B₂ solid solutions surrounding ZrB₂ pure grains, while a higher ZrC content than sample ZS was detected, Fig. 4. From thermodynamic simulations at 1900 °C and with a pressure < 1 mbar, Sc₂O₃ is not stable and, in the presence of carbon, decomposes with formation of CO and elemental Sc according to reaction (R1):

$$\text{Sc}_2\text{O}_3 + 3 \text{C} \rightarrow 2 \text{Sc} + 3 \text{CO}(\text{g}) \quad (\text{R1})$$

The elemental Sc, which at 1900 °C is liquid, spreads along the ZrB₂ grains and, taking into account that ScB₂ is isostructural with ZrB₂, it is thought that Sc atoms enter ZrB₂ lattice by substituting Zr atoms to form a solid solution, with (Zr_{0.93}Sc_{0.07})B₂ as estimated formula. On the other hand, the development of CO further promoted the formation of ZrC in the matrix.

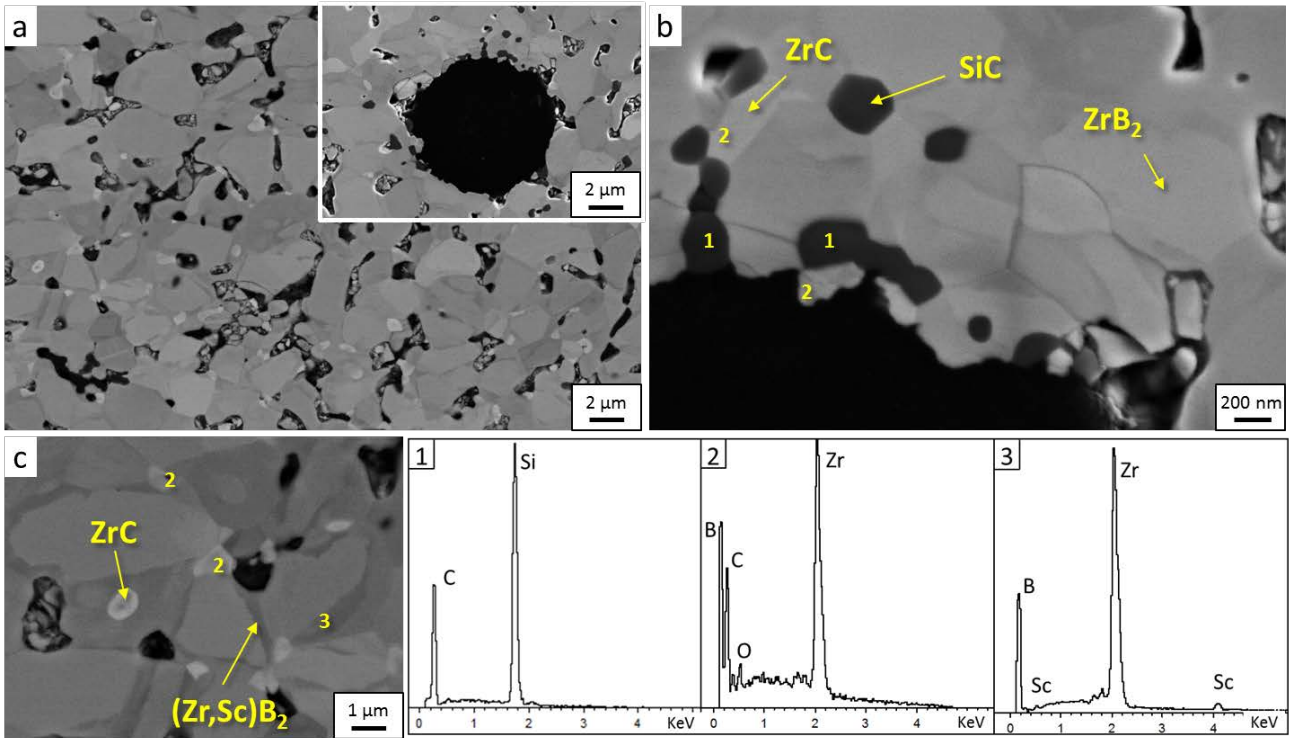


Figure 4. Microstructure of sample ZSSc: a) general view showing porosity and inset of the fibre cross section, b) detail of the fibre/matrix interface and c) ceramic matrix showing formation of (Zr,Sc)B₂ solid solution grains with EDS of the phases as labelled.

Sample **ZSY** was characterized by the lowest porosity of all samples and this was attributed to the formation of a low melting liquid phase based on a mixture of Y₂O₃, B₂O₃ and SiO₂. (Table 1). Y₂O₃ has already been reported to aid the sintering of ZrB₂ [27], but in this case we also observed the formation of new phases with a lamellar structure. These phases, with elemental composition consisting of Y, B, C in atomic ratio close to 20:40:40 plus varying amounts of oxygen, were found both at the fibre/matrix interface (Fig. 5b), or scattered in the ceramic matrix (Fig. 5c). Other phases observed were yttrium silicates found in proximity of SiC particles, which originated from the reaction (R2) between Y₂O₃ with the SiO₂ present on SiC particles, and in agreement with the phase diagrams of the Y₂O₃ – SiO₂ system [39]:



The occurrence of reaction R2 could also partially justify the lower SiC content measured by image analysis (Table 1). ZrC was found anchored to the fibres as observed for sample ZS and ZSSc.

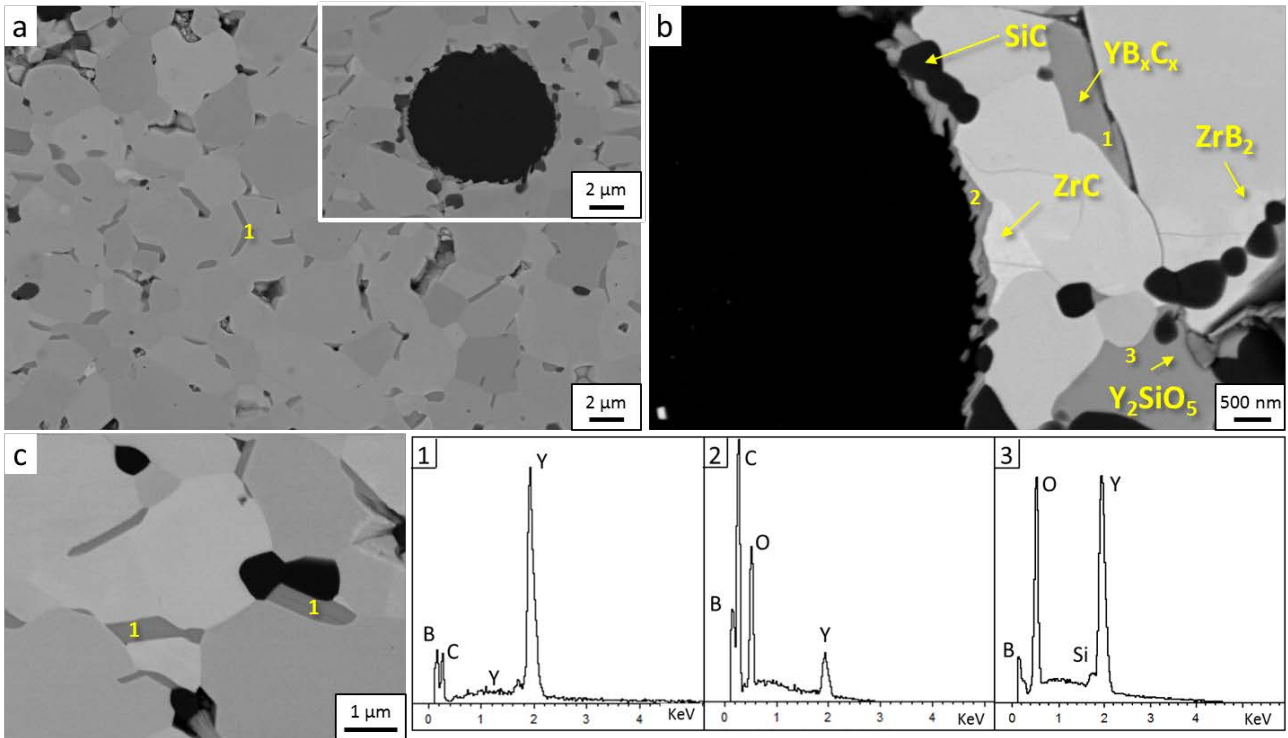


Figure 5. Microstructure of sample ZSY: a) overall view showing a dense matrix and inset of the fibre cross section, b) detail of the fibre/matrix interface with EDS of the second phases.

In view of the absence of porosity in this sample, ZSY was selected for deeper microstructure investigations. TEM analyses were carried out on this material to find out a conclusive response about the nature of the lamellar Y-B-C phase. These were extremely difficult to index because of their intrinsic anisotropy and multi-layered structure. Therefore, two typologies of samples were prepared: one from the sintered body, by conventional mechanical thinning and ion beam milling, the other by crushing the sintered pellet into powder. By combining the information obtained from the two different TEMs specimens, unambiguous identification was possible.

A low magnification overview is presented in Fig. 6a, showing the presence of the lamellar phase both scattered within the matrix, Fig. 6a,b, and surrounding the fibre, Fig. 6c,d. Punctual EDX collected in the central part of the phase revealed Y, B, O and C peaks, but in variable amounts (Fig. 6b,d). Cu and Ga were detected as grid and milling contaminations. TEM DF-HAADF and BF images showed a non-homogeneous aspect of this phase, crossed by darker O-rich filaments. The SAED pattern collected over this area and reported in Fig. 6b presents a series of aligned spots in one direction, whereas the diffraction pattern in Fig. 6c pointed to a YBO₃ phase overlapped to another crystalline phase with lower intensity spots.

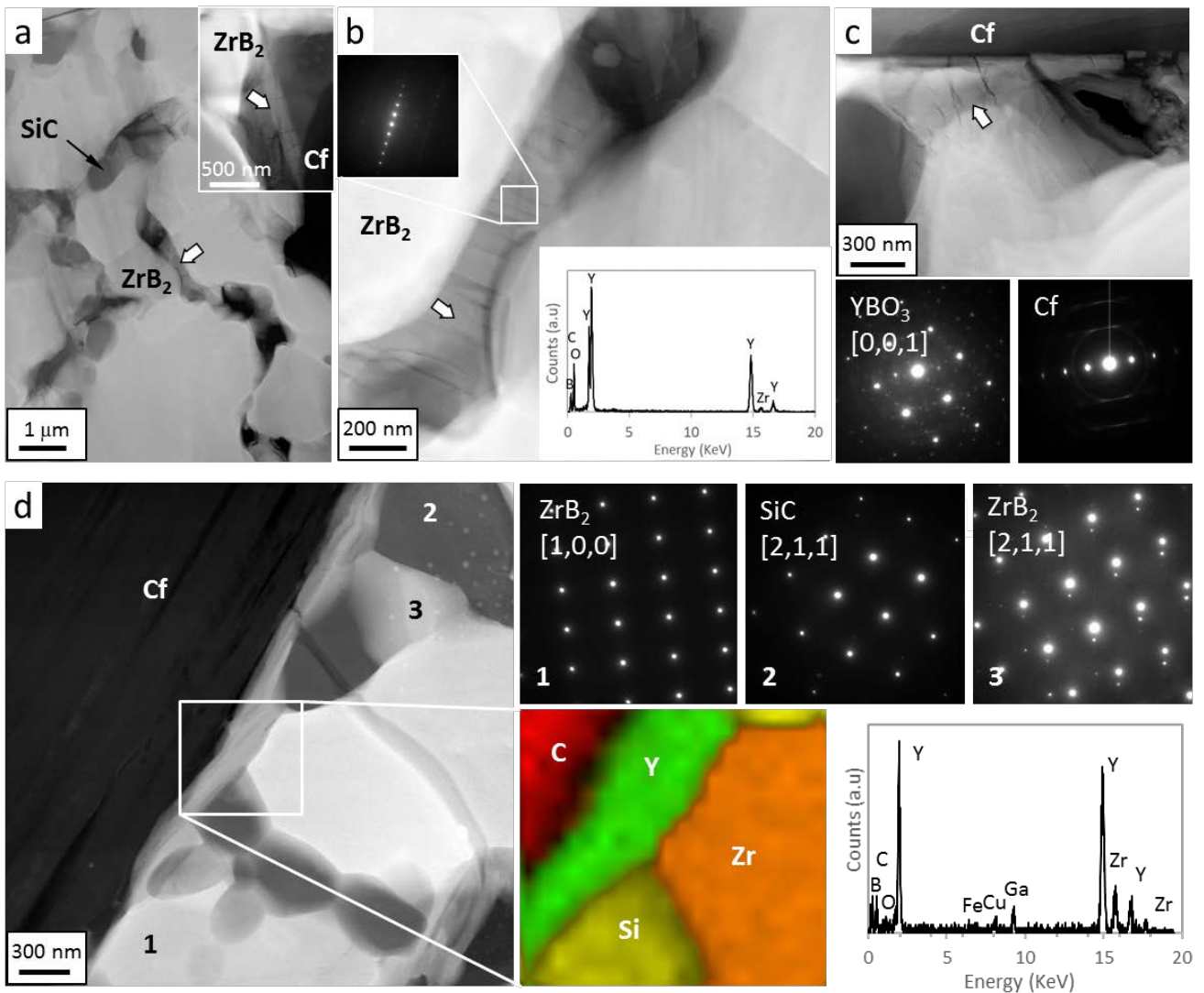


Figure 6. TEM images of the ZSY mechanically thinned specimen showing a) c) TEM images of the Y-rich lamellar phase (highlighted by white arrows) either scattered within the matrix or surrounding the fibre with corresponding EDS spectrum and diffraction pattern, and d) HAADF of a fibre-matrix interface with EDS elemental mapping of the squared area, diffraction patterns as indicated and punctual EDS spectrum of the Y-rich phase.

Further investigation by HR-TEM on a brother sample obtained by crushing method additionally pointed to a YB_2C_2 phase, Fig. 7. Upon the observed compositional variations within the lamellar phase, containing more or less oxygen, we suppose that multiple phases are present as a consequence of local chemistry variations, some of which are conducive to propose a reaction path, as discussed in section 3.4.

Lastly, in agreement with SEM analysis, in the proximity of SiC particles, Y-Si-O rich zones were observed and identified as yttrium silicate, Y_2SiO_5 , Fig. 8.

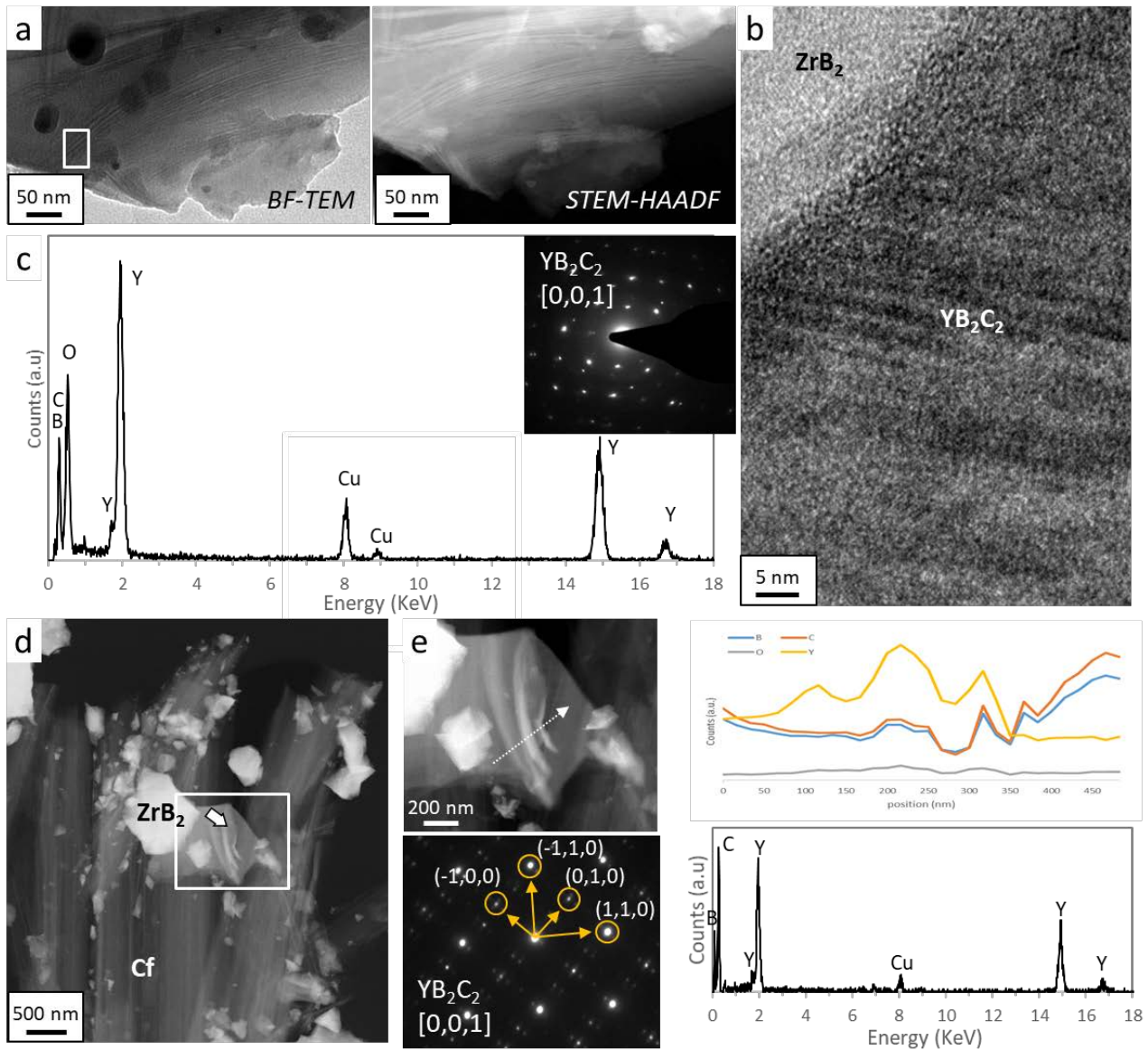


Figure 7. TEM images of the ZSY crushed specimen showing a) BF- and HAADF- images of the Y-rich lamellar phase with b) corresponding HR image and c) EDS and diffraction pattern. d) Overview of a portion of crushed material with e) magnified view of the YB_2C_2 phase covering the carbon fibre along with diffraction pattern, EDS profile (along the dotted white arrow) and punctual spectra.

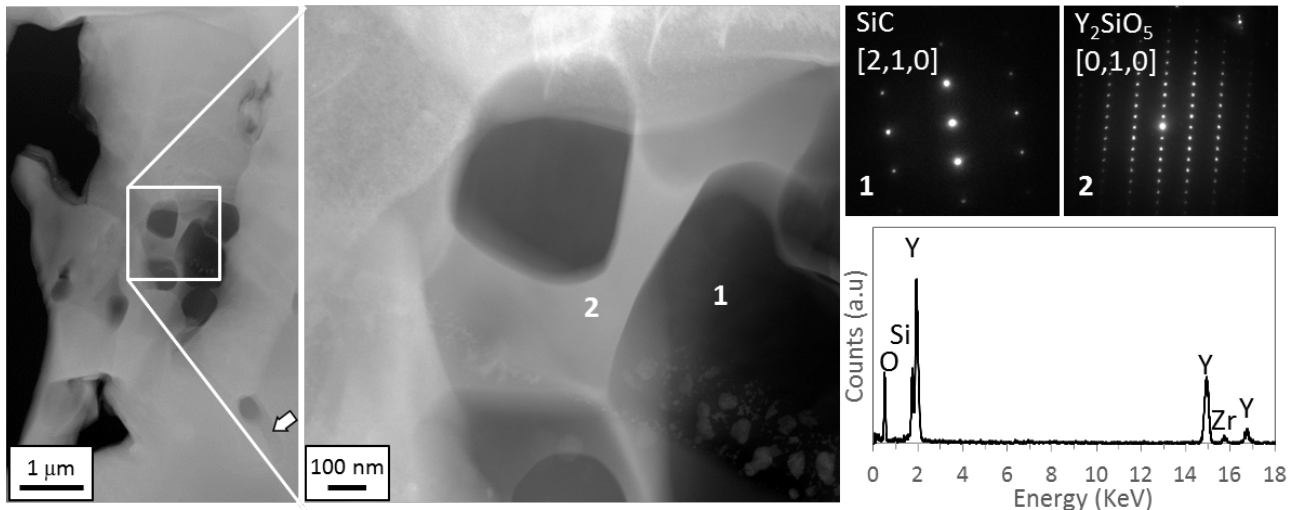


Figure 8. TEM images of the ZSY sample showing SiC surrounded by yttrium silicate with corresponding diffraction pattern and EDS spectrum. The white arrow indicates the Y-rich lamellar phase.

Sample **ZSLa** was characterized by a dense and micro-fissured matrix Fig 9a. SiC was homogeneously distributed in the matrix and lamellar phases were found at the fibre/matrix interface and occasionally between ZrB_2 grains; these had elemental composition consisting of La, B and C with varying amount of oxygen (Fig. 9b). These slight variations in oxygen content were visible in the form of differently coloured stripes around the fibres, with the darker lamellae containing more oxygen. These phases seemed to wrap the layered structure of the pitch-based fibre as can be seen in Fig. 9c. In spite of the interface reaction, the fibres still preserved their original round shape. No ZrC was observed via SEM, but its formation could not be ultimately ruled out.

TEM observations confirmed the formation of a phase containing La, B, C, around the carbon fibre, Fig. 9 d. The EDX spectrum resembled that of the YB_2C_2 phase, but with lanthanum replacing yttrium. To identify this phase, the diffraction pattern was captured, despite this crystal was placed on the fibre, whose pattern with concentric rings was preponderant, the superimposed spots identified it to be LaB_2C_2 . Combining EDX and diffraction patterns it is therefore reasonable to think that the LaB_2C_2 phase was formed around the fibres, in analogy to what was observed for the ZSY sample.

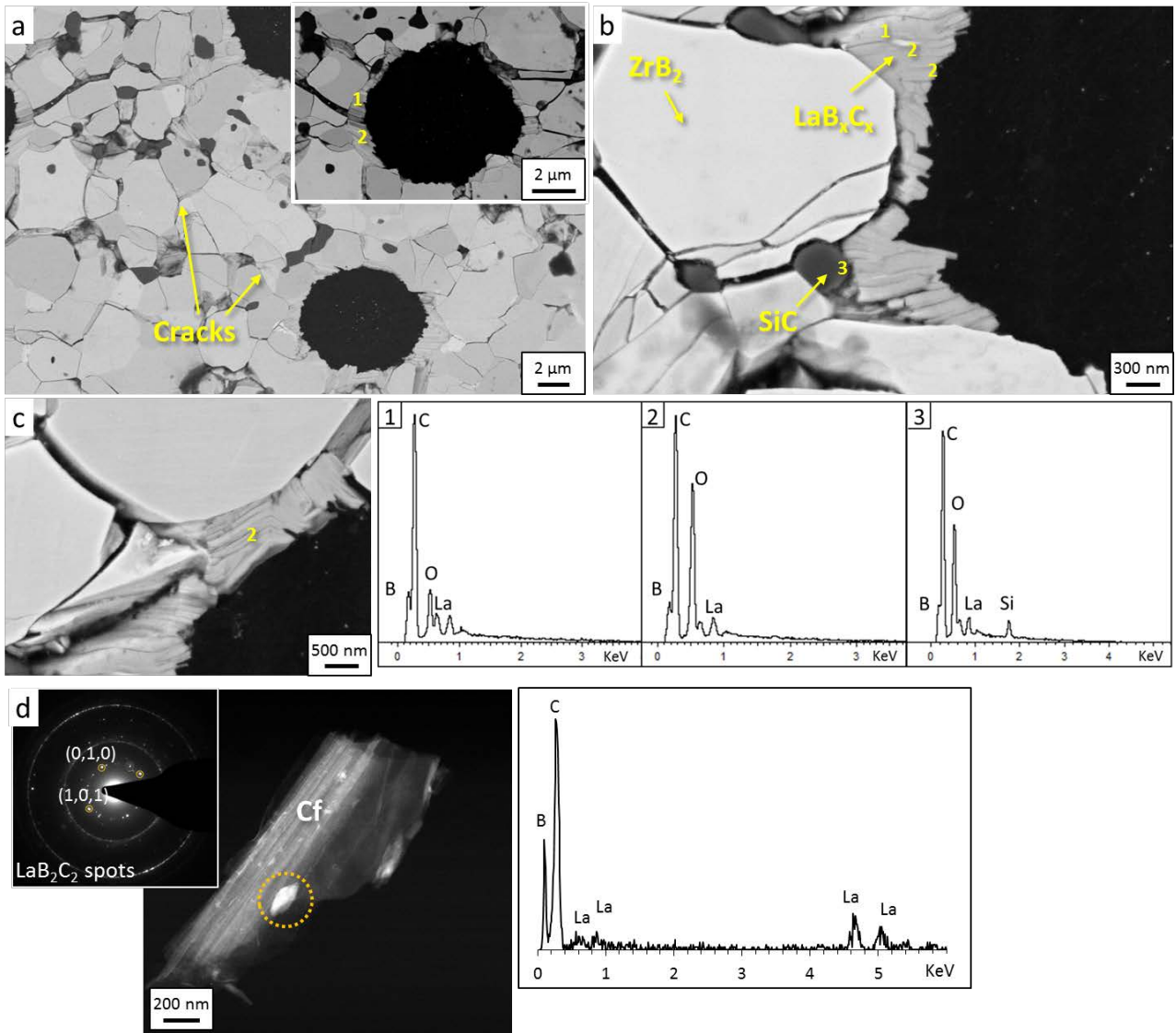


Figure 9. Microstructure of sample ZSLa: a) ceramic matrix showing a micro-fissured matrix and inset of the fibre cross section, b) detail of the fibre/matrix interface with EDS spectra of the second phases and c) detail of the lamellar phase grown on the fibre, d) TEM crushed specimen showing the punctual EDS spectrum of the La-B-C phase covering the carbon fibre along with diffraction pattern overlapped to that of the fibre underneath.

Sample **ZSCe** was more difficult to infiltrate and the final microstructure was not as homogeneous as the other specimens, particularly inhomogeneous distribution of SiC and Ce-based phases in the ZrB_2 matrix was found (Fig. 10). SiC-rich regions were mostly constituted by a ZrB_2 /SiC matrix as observed in sample ZS, without the presence of Ce phases, while in SiC-free zones, the formation of lamellar phases was observed both at the fibre/matrix interface and in the matrix. In these regions, the matrix was fully dense. Unlike other samples, fibres underwent significant degradation and consumption and it was even possible to see the preferential growth of these lamellae along the fibre graphitic layer orientations. These phases similarly contained Ce, B, C

with varying oxygen content, as can be seen from the different grey scales of the stripes around the fibres, but quantification of the individual elements was not possible due to the large difference in atomic number. EDS analysis on ZrB_2 grains did not detect any Ce trace, suggesting that no solid solution was formed.

After a week of exposure to ambient atmosphere, the sample underwent notable swelling and cracking, suggesting that the newly formed phases were not stable in air.

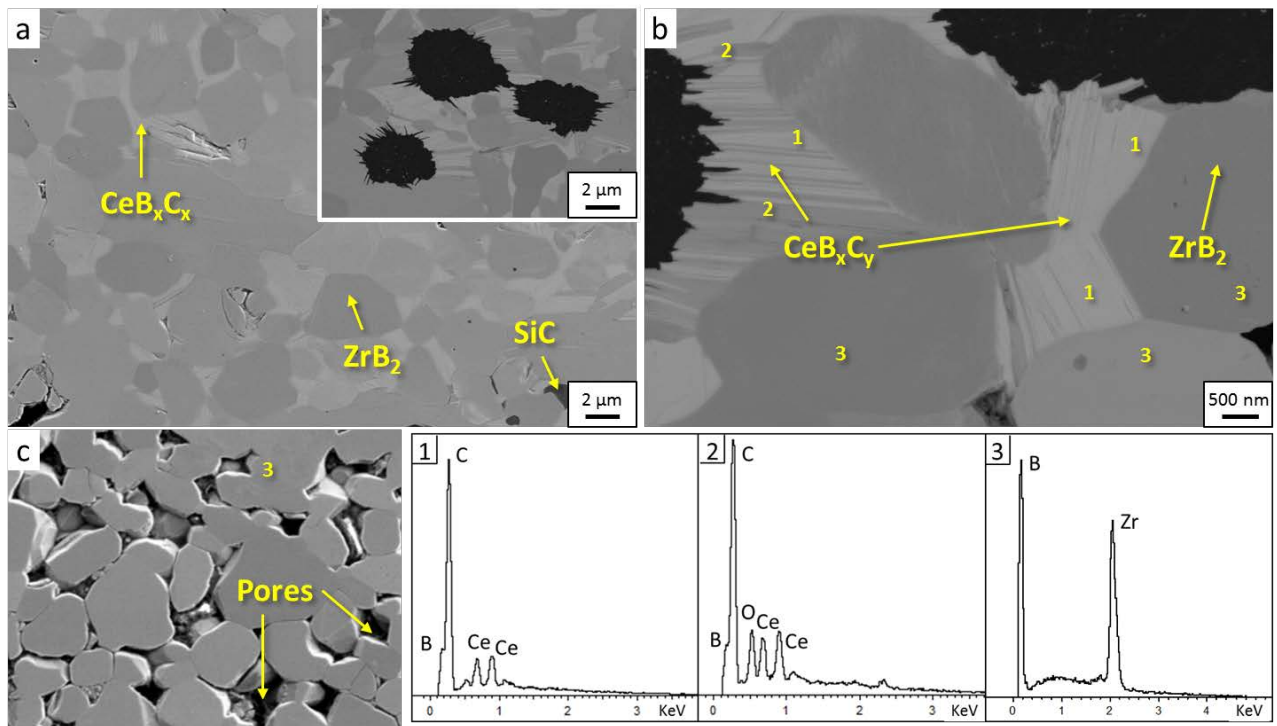


Figure 10. Microstructure of sample ZSCe: a) fully dense Ce-rich ceramic matrix and inset of the fibre cross section, b) detail of the fibre/matrix interface with morphology of the CeB_xC_y new phase and c) Ce-free porous matrix with EDS of the corresponding phases.

3.3 Mechanical properties

Mechanical properties are reported in Table 2. Sample ZSCe could not be tested because of severe degradation upon exposure to air, but in all other cases, doping with a REO led to a general increase of all properties as compared to the ZS baseline.

Table 2. Microstructural features and values of flexural strength (σ) measured at room temperature and 1500°C in Ar, and fracture toughness (K_{Ic}). Values for ZS and ZSY are taken from [28]

Sample	Fibre (vol%)	Porosity (vol%)	$\sigma_{25^\circ\text{C}}$ (MPa)	$\sigma_{1500^\circ\text{C}}$ (MPa)	K_{Ic} (MPa·m ^{0.5})
ZS	47.9	5.9	283 ± 23	451 ± 25	8.0 ± 0.3
ZSSc	46.7	5.8	335 ± 13	640 ± 81	10.8 ± 0.9
ZSY	50.4	0.9	436 ± 20	709 ± 88	11.5 ± 0.7
ZSLa	50.9	4.7	360 ± 117	626 ± 28	16.5 ± 0.9

Room temperature flexural strength for all samples was in the 300-400 MPa range, with increasing strengths with the decrease of porosity. With reference to the ZS sample, the REO-containing composites had strength around 100 MPa and up to around 200 MPa higher upon testing at room temperature and at 1500°C in argon atmosphere, respectively. Considerable scattering was observed for sample ZSLa, possibly due to micro-cracking, Fig. 9a. Tests carried out at 1500°C showed indeed an increase in strength of ~60% as compared to the room temperature values for all materials, accompanied by a change in the fracture behaviour from graceful to brittle, Fig. 11. This phenomenon had already been observed in previous works and was attributed to the relaxation of stresses [40]. Looking at the load-displacement curves in Fig. 11b, at high temperature, all samples exhibited a linear behaviour up to fracture. The baseline sample, ZS, and ZSSc were characterized by a small flex between 50 – 100 N (decrease in slope) at room temperature, Fig. 11a. This flex was hardly visible for ZSY and ZSLa. In these UHTCMCs, unlike carbon fibre reinforced polymers (CFRPs), the moduli of the ceramic matrix and the fibre reinforcement are comparable, and the behaviour of the matrix is significant for fibre contents < 40 vol% [41]. Therefore, for samples ZS and ZSSc, the early flex could be attributed to premature rupturing of the ceramic matrix, followed by the load transfer to the fibres. For samples ZSY and ZSLa, which contain more than 50 vol% carbon fibres, the curve behaviour was mostly dominated by the fibre reinforcement that bore the load together with the matrix till rupture occurred. For sample ZSLa, a change in the slope was observed at low loads, possibly in relation to the micro-cracking already present after sintering.

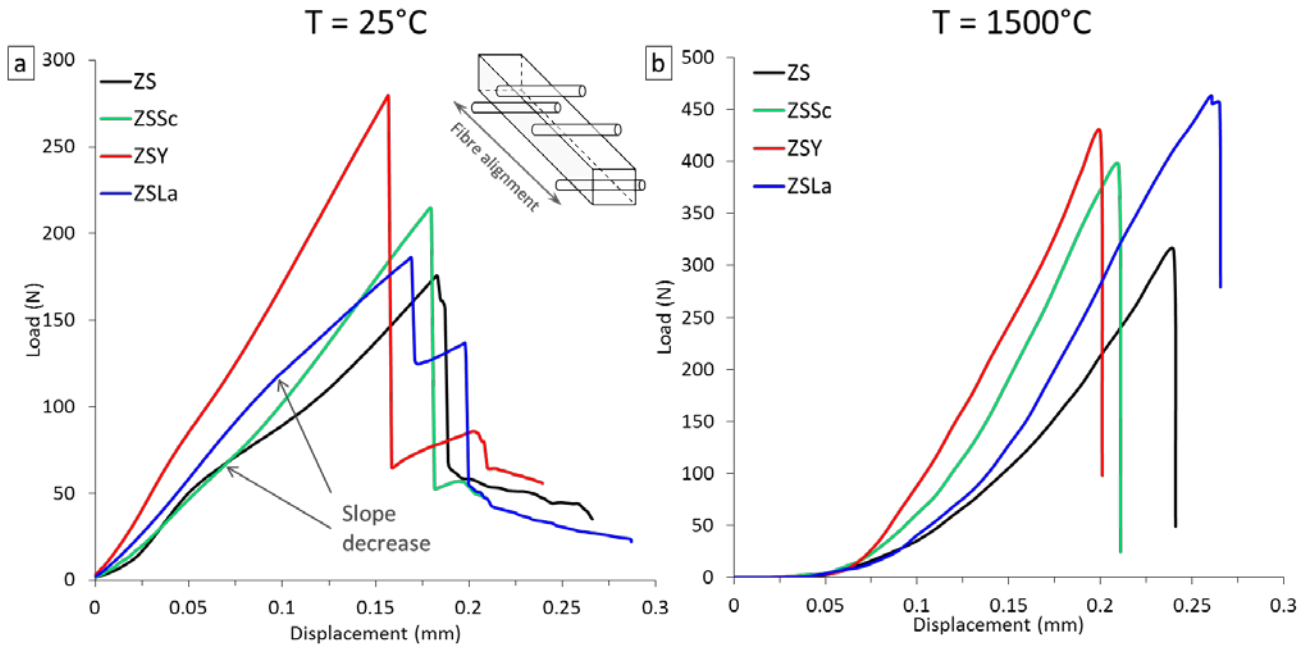


Figure 11. Load-displacement curves for 4-point strength measured on the baseline and REO-doped composites a) at room temperature with sketch of the material testing apparatus and fibre orientation inset and b) at 1500°C in argon atmosphere.

All samples exhibited a graceful fracture, as demonstrated by the load-displacement curves during chevron-notch tests in Fig. 12. Fracture toughness was similar for ZSSc and ZSY samples, 10-11 MPa·m^{0.5}, considerably higher than the reference ZS, ~8 MPa·m^{0.5}. Remarkable values were achieved for ZSLa, approaching 17 MPa·m^{0.5}. These differences can be firstly attributed to the fibre volume fraction, close to 50 vol% for ZSLa and ZSY, versus 46-47 vol% for ZS and ZSSc. Another factor could be the porosity, below 1% for ZSY or 4-6 vol% for the other composites, however this parameter, within these levels, seems not to have a direct impact on the fracture toughness. The third component that promoted toughness increase could be the lamellar phase which could have acted as additional compliant phase, similar to MAX phases, i.e. analogous layered ternary carbides and nitride where formation of kink bands and bridging among the planes are responsible for a failure tolerant behaviour [42].

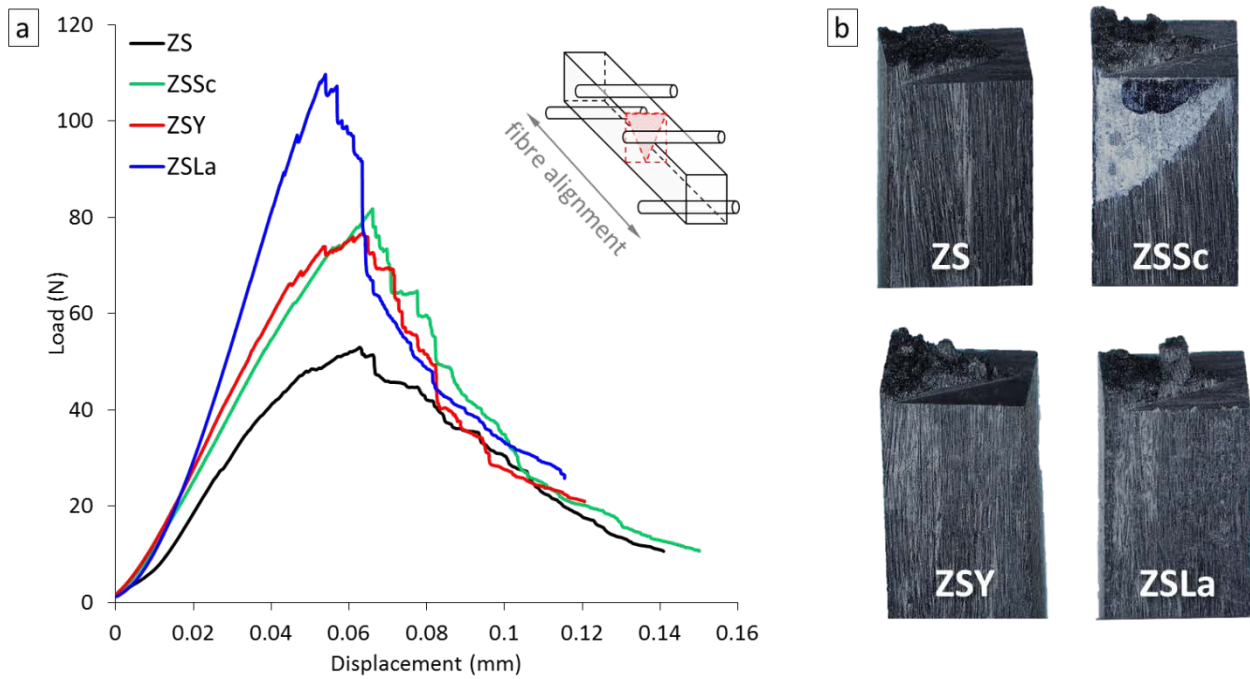


Figure 12. a) Load-displacement curves for CNB tests measured at room temperature on the baseline and REO-doped composites with b) photo of the broken specimens showing different fracture behaviour.

Looking at the fracture surfaces of these materials, Fig. 12b and 13, the fibres appeared well anchored to the matrix in all specimens with fibre pull-out only in the order of 5-10 μm . Here and in previous work [28], we observed how the outer layer of the pitch fibre had reacted with the matrix, but the fibre could still slide within its own layers. In the case of sample ZSLa, this outer layer appeared fully transformed in the lamellar phase, that might have played a key role promoting fibre sliding.

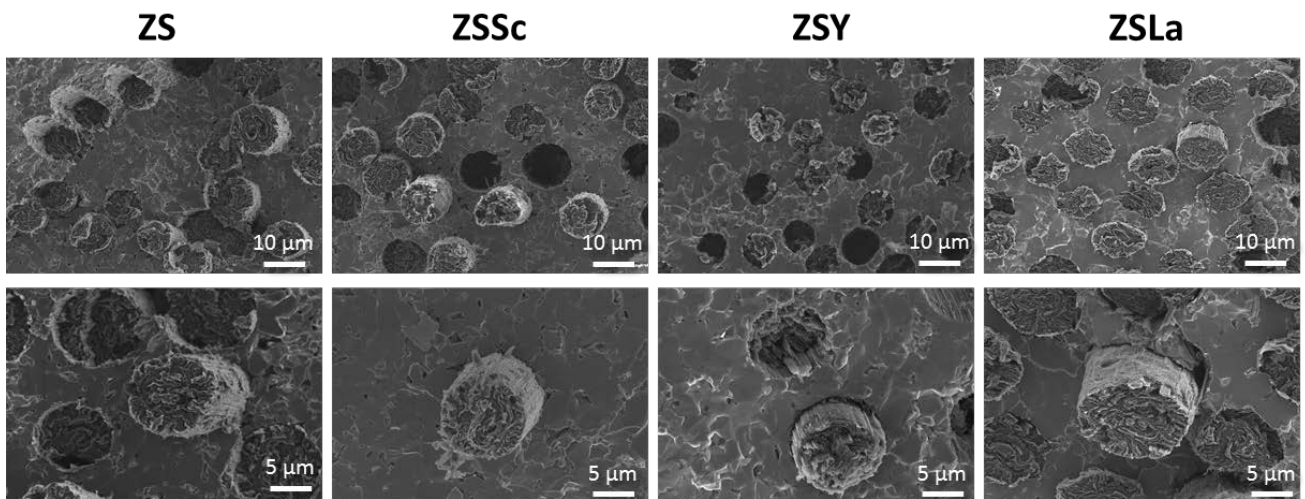


Figure 13. SEM images of the fractured surface of the REO-doped composites at low (above) and high (bottom) magnification.

3.4 Role of REO on the microstructure and properties of UHTCMCs

The sintering mechanism for the REO-doped materials was principally attributed to liquid phase sintering: the REO forms a mixture with the oxides present on the surface of ZrB₂ and SiC particles, such as B₂O₃ and SiO₂, and spreads within the composite. Taking Y₂O₃ as example, according to the phase diagrams of the Y₂O₃ – B₂O₃ system [43], a eutectic is predicted at a temperature as low as 1373°C for 70 mol% of B₂O₃. La₂O₃ and Sc₂O₃ can form a eutectic at 1141°C[44] and 1526°C [45], respectively for 70 mol% of B₂O₃. All the REOs investigated can form the corresponding borate phase which has a congruent melting point of ~1650°C [46].

Based on the microstructural observations, reaction intermediates were found, like the YBO₃ crystalline phase, Fig. 6c. This is the reaction product of the direct interaction between REO and boron oxide, as expressed by reaction (R3):



This phase, depending on the local chemistry and proximity to carbon sources as fibre or fibre debris, can then undergo carbo-reduction until reaching a stable YB₂C₂ phase, according to reactions (R4-R7):



These reactions clearly evidence the cleaning effect of the REO on the boride particles, but also point out remarkable development of gaseous phase, possibly explaining around 5vol% porosity in the final composite.

B₂O₃ is likely to form liquid phases with SiO₂ too, which can have melting points ranging from 372 °C to 1482°C depending on the mol% of B₂O₃, rendering the entire oxide mixture more available for further reactions with carbon [47].

What emerges from the SEM and TEM observations is that by adding lanthana, ceria and yttria to the ZS matrix, the formation of a multi-layered phase with the generic formula REB₂C₂ is promoted. Only in the case of scandia, this did not happen, and it was instead observed that scandium tended to form a (Zr,Sc)B₂ solid solution inside the grains of ZrB₂. A possible explanation for this phenomenon can be found using Hume-Rothery's rule for the solid solutions: if a solute differs in its atomic size by more than about 15% from the host, then it is likely to have a low solubility, i.e. the "size factor" is said to be unfavourable. Comparing the atomic radii of the various elements involved, Sc, Y, La and Ce with that of Zr, it emerges that only scandium is likely to form solid solutions with ZrB₂, with a difference of below 1%. On the other hand, Y, La and Ce are characterized by a much larger atomic radius compared to zirconium and close to the critical 15% value, these being equal to 13%, 18% and

14%, respectively. Another factor to take into consideration is the electronegativity of the elements involved. If a solute has a large difference in electronegativity when compared with the host, then it is more likely to form a compound. Its solubility in the host would therefore be limited. Also in this case, scandium is the element most susceptible to formation of solid solutions having electronegativity very similar to zirconium, 1.36 against 1.33 [48]. These reasons might have led the scandium to form the (Zr,Sc)B₂ solid solution around ZrB₂ cores, rather than the analogous ScB₂C₂ phase at the fibre matrix interface.

According to the phase diagrams of the REO – SiO₂ systems, all these behave in a very similar way, forming the corresponding silicate between 1770°C – 1980°C, but in the present study, silicates were observed only for ZSY [39]. Considering the strict ranges over which these phases are stable, this discrepancy could be attributed to the different local stoichiometry that did not allow for the formation of such phases and the retention of SiC.

As far as the role of these lamellar phases is concerned in affecting the mechanical properties, it is difficult to tell whether the increase in flexural strength is due to the presence of these phases or to the reduction of porosity. A possible effect could be stress relaxation due to the lower CTE that allows these phases to act as compliant phase between ZrB₂ grains, or between the fibre and the matrix, but few data are available regarding the thermal properties of these compounds, so no ultimate speculations can be done.

If we exclude the ZSY material that had almost no porosity, we can make comparisons keeping fixed the porosity and fibre fraction parameters. Taking composites with the same level of porosity, 5.8 – 5.9%, and fibre, 46 – 48 vol%, like ZS and ZSc, notable improved strengths were found for the Sc-doped material. For ZSSc no lamellar phase was found, but a (Zr,Sc)B₂ solid solution-rich ceramic matrix formed, which could have promoted strength increase at high temperature, like observed in analogous bulk matrices exhibiting the solid solution feature around the original ZrB₂ grain seeds [49][50]. In comparison with the material with higher fibre amount, 50 vol%, and the same porosity level, ZSLa, achieved similar strength and the highest fracture toughness, 16-17 MPa·m^{0.5}. Since the fully dense ZSY with the same 50 vol% fibre achieved a fracture toughness between 11-12 MPa·m^{0.5}, we can speculate that the additional increment is given both by the lamellar phase and its ductile behaviour bridging the crack advancement and the micro-crack toughening operating within the ceramic matrix.

Another property, not examined in the present work, but that could benefit from the introduction of REO into the ZrB₂-SiC ceramic system is the ablation resistance. Exposure to oxygen will convert the boro-carbides back to the REO and B₂O₃. All these REOs have got melting points above 2100°C, being Sc₂O₃ the highest, 2485°C, and could therefore be a suitable ablation resistant

material. In addition, all 8-10 mol% REO have a positive effect on the stabilization of ZrO_2 in the tetragonal structure, the volume expansion associated to the martensitic transition is avoided and thus cracking of the oxide scale is limited with benefits on the overall architecture integrity.

However, in the first instance, the oxidation resistance will depend on which oxide promotes the formation of a dense matrix and of a compact ZrO_2 outermost layer. According to the phase diagrams of REO– ZrO_2 systems, Sc_2O_3 and Y_2O_3 form an eutectic at $\sim 2400^\circ C$ with ZrO_2 , implying that such phases would be active only under extreme temperatures, whereas La_2O_3 is able to form an eutectic already at $2070^\circ C$, making it more promising for the oxidation in milder conditions[51]. Preliminary results on the oxidation resistance of Y_2O_3 -doped ZrB_2/SiC composites at $1650^\circ C$ have shown that the presence of Y_2O_3 ultimately led to the formation of YBO_3 which spread around the ZrO_2 grains, filling the gaps. However in that work, the overall low SiO_2 content, deriving from SiC consumption during sintering, led to a slightly lower performance than the REO-free composites [28]. Further studies on samples containing a higher SiC content have instead demonstrated the efficacy of Y_2O_3 in improving the oxidation resistance [52][53].

4. Conclusions

The influence of group IIIb rare earth oxides (REOs) on the microstructure and mechanical properties of carbon fibre reinforced- ZrB_2/SiC composites was investigated. In all cases, the addition of 5 vol% REO led to a porosity decrease which was accompanied by an increase in flexural strength and toughness. Addition of Y_2O_3 , La_2O_3 and Ce_2O_3 effectively cleaned the boride grains from the oxide covering the raw powders and led to the formation of lamellar ternary compounds containing the RE metal, boron and carbon; confirmed by TEM analysis to belong to a class of ternary boro-carbides of general formula REB_2C_2 . Sc_2O_3 was instead preferably consumed to form $(Zr,Sc)B_2$ solid solution shell structures around ZrB_2 cores in the matrix.

Taking into account the significant improvement of high temperature strength, achieving over 630 MPa, and 16 MPam^0 of fracture toughness for the samples containing these lamellar phases, which almost doubled as compared to the reference REO-free composite, it is likely that they play a role in the load transfer mechanism and promote toughening mechanisms, like bridging of the kink bands.

Acknowledgements

This work has received funding from the European Union’s Horizon 2020 “Research and innovation programme” under grant agreement N°685594 (C³HARME). TEM investigations were sponsored by the U.S. Army DEVCOM and accomplished under the Cooperative Agreement n. W911NF-19-2-0253 with Amanda Napier as contract monitor. The views and conclusions contained in this document

are those of the authors and should not be interpreted as representing the official policies, either expressed or implied, of the U.S. Army DEVCOM or the U.S. Government. The U. S. Government is authorized to reproduce and distribute reprints for Government purposes notwithstanding any copyright notation herein. The authors wish to thank Simone Failla for sintering cycles, Cesare Melandri and Pietro Galizia for mechanical testing, and Claudio Capiani for XRD analysis.

References

- [1] H. Hald, Operational limits for reusable space transportation systems due to physical boundaries of C/SiC materials, *Aerosp. Sci. Technol.* 7 (2003) 551–559. doi:10.1016/S1270-9638(03)00054-3.
- [2] W.G. Fahrenholtz, E.J. Wuchina, W.E. Lee, Z. Y., eds., *Ultra-High Temperature Ceramics: Materials for Extreme Environment Applications*, John Wiley & Sons, 2014.
- [3] W.G. Fahrenholtz, E.J. Wuchina, W.E. Lee, Y. Zhou, eds., *Ultra-High Temperature Ceramics: Materials for Extreme Environment Applications*, John Wiley & Sons Inc., Hoboken, New Jersey, 2014. doi:10.1002/9781118700853.
- [4] M.M. Opeka, I.G. Talmy, E.J. Wuchina, J. a. Zaykoski, S.J. Causey, Mechanical, Thermal, and Oxidation Properties of Refractory Hafnium and zirconium Compounds, *J. Eur. Ceram. Soc.* 19 (1999) 2405–2414. doi:10.1016/S0955-2219(99)00129-6.
- [5] J. Han, P. Hu, X. Zhang, S. Meng, Oxidation behavior of zirconium diboride-silicon carbide at 1800 °C, *Scr. Mater.* 57 (2007) 825–828. doi:10.1016/j.scriptamat.2007.07.009.
- [6] T.A. Parthasarathy, R.A. Rapp, M. Opeka, R.J. Kerans, A model for the oxidation of ZrB₂, HfB₂ and TiB₂, *Acta Mater.* 55 (2007) 5999–6010. doi:10.1016/j.actamat.2007.07.027.
- [7] J. Zou, V. Rubio, J. Binner, Thermoablative resistance of ZrB₂-SiC-WC ceramics at 2400°C, *Acta Mater.* 133 (2017) 293–302.
- [8] D. Sciti, L. Silvestroni, F. Monteverde, A. Vinci, L. Zoli, Introduction to H2020 project C3HARME—next generation ceramic composites for combustion harsh environment and space, *Adv. Appl. Ceram.* (2018). doi:10.1080/17436753.2018.1509822.
- [9] L. Zoli, D. Sciti, A. Vinci, P. Galizia, F. Monteverde, S. Failla, L. Silvestroni, Ultra-High Temperature Ceramic Matrix Composites, in: *Encycl. Mater. Tech. Ceram. Glas.*, Elsevier, 2021: pp. 340–352. doi:10.1016/b978-0-12-818542-1.00023-0.
- [10] J. Binner, M. Porter, B. Baker, J. Zou, V. Venkatachalam, V.R. Diaz, A. D’Angio, P. Ramanujam, T. Zhang, T.S.R.C. Murthy, Selection, processing, properties and applications of ultra-high temperature ceramic matrix composites, UHTCMCs—a review, *Int. Mater. Rev.* 65 (2020) 389–444. doi:10.1080/09506608.2019.1652006.

- [11] H. Jin, S. Meng, W. Xie, C. Xu, J. Niu, ZrB₂-CNTs Nanocomposites Fabricated by Spark Plasma Sintering, *Materials (Basel)*. 9 (2016) 967. doi:10.3390/ma9120967.
- [12] D. Sciti, L. Pienti, A. Natali Murri, E. Landi, V. Medri, L. Zoli, From random chopped to oriented continuous SiC fibers-ZrB₂ composites, *Mater. Des.* 63 (2014) 464–470. doi:10.1016/j.matdes.2014.06.037.
- [13] S. Guicciardi, L. Silvestroni, M. Nygren, D. Sciti, Microstructure and toughening mechanisms in spark plasma-sintered ZrB₂ ceramics reinforced by SiC whiskers or SiC-chopped fibers, *J. Am. Ceram. Soc.* 93 (2010) 2384–2391. doi:10.1111/j.1551-2916.2010.03730.x.
- [14] Y. Zhu, S. Wang, W. Li, S. Zhang, Z. Chen, Preparation of carbon fiber-reinforced zirconium carbide matrix composites by reactive melt infiltration at relative low temperature, *Scr. Mater.* 67 (2012) 822–825. doi:10.1016/j.scriptamat.2012.07.044.
- [15] D. Sciti, A. Natali Murri, V. Medri, L. Zoli, Continuous C fibre composites with a porous ZrB₂ Matrix, *Mater. Des.* 85 (2015) 127–134. doi:10.1016/j.matdes.2015.06.136.
- [16] L. Zoli, A. Vinci, P. Galizia, C. Melandri, Di. Sciti, On the thermal shock resistance and mechanical properties of novel unidirectional UHTCMCs for extreme environments, *Sci. Rep.* 8 (2018) 1–9. doi:10.1038/s41598-018-27328-x.
- [17] P. Galizia, S. Failla, L. Zoli, D. Sciti, Tough salami-inspired Cf/ZrB₂ UHTCMCs produced by electrophoretic deposition, *J. Eur. Ceram. Soc.* 38 (2018) 403–409. doi:10.1016/J.JEURCERAMSOC.2017.09.047.
- [18] D. Sciti, L. Zoli, A. Vinci, L. Silvestroni, S. Mungiguerra, P. Galizia, Effect of PAN-based and pitch-based carbon fibres on microstructure and properties of continuous Cf/ZrB₂-SiC UHTCMCs, *J. Eur. Ceram. Soc.* (2020). doi:10.1016/j.jeurceramsoc.2020.05.032.
- [19] D. Sciti, P. Galizia, T. Reimer, A. Schoberth, C.F. Gutiérrez-Gonzalez, L. Silvestroni, A. Vinci, L. Zoli, Properties of large scale ultra-high temperature ceramic matrix composites made by filament winding and spark plasma sintering, *Compos. Part B Eng.* 216 (2021). doi:10.1016/j.compositesb.2021.108839.
- [20] L. Silvestroni, A. Vinci, S. Failla, L. Zoli, V. Rubio, J. Binner, D. Sciti, Ablation behaviour of ultra-high temperature ceramic matrix composites: Role of MeSi₂ addition, *J. Eur. Ceram. Soc.* 39 (2019). doi:10.1016/j.jeurceramsoc.2019.03.031.
- [21] R. Savino, M. De Stefano, L. Silvestroni, D. Sciti, Arc-jet testing on HfB₂ and HfC-based ultra-high temperature ceramic materials, 28 (2008) 1899–1907. doi:10.1016/j.jeurceramsoc.2007.11.021.
- [22] S. Mungiguerra, G.D. Di Martino, R. Savino, L. Zoli, D. Sciti, M.A. Lagos, Ultra-High-

Temperature Ceramic Matrix Composites in Hybrid Rocket Propulsion Environment, in: 2018 Int. Energy Convers. Eng. Conf., American Institute of Aeronautics and Astronautics, 2018. doi:doi:10.2514/6.2018-4694.

- [23] L.M. Rueschhoff, C.M. Carney, Z.D. Apostolov, M.K. Cinibulk, Processing of fiber-reinforced ultra-high temperature ceramic composites: A review, *Int. J. Ceram. Eng. Sci.* 2 (2020) 22–37. doi:10.1002/ces2.10033.
- [24] L. Zoli, A. Vinci, P. Galizia, C.F. Gutiérrez-Gonzalez, S. Rivera, D. Sciti, Is spark plasma sintering suitable for the densification of continuous carbon fibre - UHTCMCs?, *J. Eur. Ceram. Soc.* (2019). doi:10.1016/j.jeurceramsoc.2019.12.004.
- [25] L. Zoli, A. Vinci, L. Silvestroni, D. Sciti, M. Reece, S. Grasso, Rapid spark plasma sintering to produce dense UHTCs reinforced with undamaged carbon fibres, *Mater. Des.* 130 (2017). doi:10.1016/j.matdes.2017.05.029.
- [26] A. Li, J. Zhang, F. Zhang, L. Li, S. Zhu, Y. Yang, Effects of fiber and matrix properties on the compressive strength of carbon fiber reinforced polymer composites, *Carbon N. Y.* 176 (2021) 652. doi:10.1016/j.carbon.2021.02.036.
- [27] X. Zhang, X. Li, J. Han, W. Han, C. Hong, Effects of Y₂O₃ on microstructure and mechanical properties of ZrB₂-SiC ceramics, *J. Alloys Compd.* 465 (2008) 506–511. doi:10.1016/j.jallcom.2007.10.137.
- [28] A. Vinci, L. Zoli, P. Galizia, D. Sciti, Influence of Y₂O₃ addition on the mechanical and oxidation behaviour of carbon fibre reinforced ZrB₂/SiC composites, *J. Eur. Ceram. Soc.* (2020). doi:10.1016/j.jeurceramsoc.2020.06.043.
- [29] G. Zhao, J. Chen, Y. Li, M. Li, YB₂C₂: A machinable layered ternary ceramic with excellent damage tolerance, *Scr. Mater.* 124 (2016) 86–89. doi:10.1016/j.scriptamat.2016.06.041.
- [30] Y. Zhou, H. Xiang, X. Wang, W. Sun, F.Z. Dai, Z. Feng, Electronic structure and mechanical properties of layered compound YB₂C₂: A promising precursor for making two dimensional (2D) B₂C₂ nets, *J. Mater. Sci. Technol.* 33 (2017) 1044–1054. doi:10.1016/j.jmst.2016.09.028.
- [31] Y. Yang, T. Hong, Mechanical and thermodynamic properties of YB₂C₂ under pressure, *Phys. B Condens. Matter.* 525 (2017) 154–158. doi:10.1016/j.physb.2017.09.026.
- [32] T. Sakai, G.-Y. Adachi, J. Shiokawa, Electrical properties of rare earth diborodiborides (RB₂C₂-type layer compounds), *J. Less Common Met.* 84 (1982) 107–114. doi:https://doi.org/10.1016/0022-5088(82)90134-5.
- [33] M. Chen, X. Hu, K. Li, J. Sun, Z. Liu, B. An, X. Zhou, Z. Liu, Self-assembly of dendritic-lamellar MXene/Carbon nanotube conductive film for wearable tactile sensors and artificial

- skin, Carbon N. Y. 164 (2020) 111–120. doi:10.1016/j.carbon.2020.03.042.
- [34] H. Chen, H. Xiang, F. Dai, J. Liu, Y. Zhou, High strength and high porosity YB₂C₂ ceramics prepared by a new high temperature reaction/ partial sintering process, J. Mater. Sci. Technol. 35 (2019) 2883–2891. doi:https://doi.org/10.1016/j.jmst.2018.09.071.
- [35] G.S. Smith, Q. Johnson, P.C. Nordine, The crystal structure of ScB₂C₂, Acta Crystallogr. 19 (1965) 668–673. doi:https://doi.org/10.1107/S0365110X65004061.
- [36] J. van Duijn, K. Suzuki, J.P. Attfield, Boron – Carbon Order in CeB₂C₂, Angew. Chemie Int. Ed. 39 (2000) 365–366. doi:https://doi.org/10.1002/(SICI)1521-3773(20000117)39:2<365::AID-ANIE365>3.0.CO;2-Q.
- [37] A. Vinci, L. Zoli, D. Sciti, C. Melandri, S. Guicciardi, Understanding the mechanical properties of novel UHTCMCs through random forest and regression tree analysis, Mater. Des. 145 (2018) 97–107. doi:10.1016/j.matdes.2018.02.061.
- [38] G. Peng, K. Li, X. Zhong, G. Li, W. Li, J. Bao, J. Wang, Mechanical properties of unidirectional carbon fiber composites based on domestic T800H carbon fiber, M40J graphite fiber and their mixtures, Carbon N. Y. 176 (2021) 653. doi:10.1016/j.carbon.2021.02.039.
- [39] Phase Equilibria Diagrams Online Database (NIST Standard Reference Database 31), The American Ceramic Society and the National Institute of Standards and Technology, 2021. Figure Numbers 2372, 2388, 2384; www.nist.gov/srd/nist31.cfm, (n.d.).
- [40] A. Vinci, L. Zoli, D. Sciti, J. Watts, G.E. Hilmas, W.G. Fahrenholtz, Mechanical behaviour of carbon fibre reinforced TaC/SiC and ZrC/SiC composites up to 2100°C, J. Eur. Ceram. Soc. 39 (2019). doi:10.1016/j.jeurceramsoc.2018.11.017.
- [41] L. Silvestroni, UHTCMCs: short vs continuous fibers, in: Ultra-High Temp. Ceram. Mater. Extrem. Environ. Appl. III, Gold Coast, Australia, 2015.
- [42] B.M. Radovic, M.W. Barsoum, MAX phases : Bridging the gap between metals and ceramics, Am. Ceram. Soc. Bull. 92 (2013) 20–27.
- [43] E.M. Levin, Liquid Immiscibility in Oxide Systems, in: A.M. Alper (Ed.), Phase Diagrams, Vol. 3, Academic Press, New York, NY, n.d.: pp. 143–236.
- [44] E.M. Levin, C.R. Robbins, J.L. Waring, Immiscibility and the System Lanthanum Oxide–Boric Oxide, J. Am. Ceram. Soc. 44 (1961) 87–91.
- [45] E.M. Levin, Structural Interpretation of Immiscibility in Oxide Systems: IV, Occurrence, Extent, and Temperature of the Monotectic, J. Am. Ceram. Soc. 50 (1967) 53–54.
- [46] Phase Equilibria Diagrams Online Database (NIST Standard Reference Database 31), The American Ceramic Society and the National Institute of Standards and Technology, 2021.

Figure Numbers 321, 4390, 2352; www.nist.gov/srd/nist31.cfm, (n.d.).

- [47] Phase Equilibria Diagrams Online Database (NIST Standard Reference Database 31), The American Ceramic Society and the National Institute of Standards and Technology, 2021. Figure Numbers 6455; www.nist.gov/srd/nist31.cfm, (n.d.).
- [48] J.E. Huheey, E.A. Keiter, R.L. Keiter, *Inorganic chemistry : principles of structure and reactivity*, HarperCollins College Publishers, New York, NY, 1993.
- [49] L. Silvestroni, H.-J. Kleebe, W.G. Fahrenholtz, J. Watts, Super-strong materials for temperatures exceeding 2000 °C, *Sci. Rep.* 7 (2017) 40730. doi:10.1038/srep40730.
- [50] L. Silvestroni, N. Gilli, A. Migliori, D. Sciti, J. Watts, G.E. Hilmas, W.G. Fahrenholtz, A simple route to fabricate strong boride hierarchical composites for use at ultra-high temperature, *Compos. Part B Eng.* 183 (2020) 107618. doi:<https://doi.org/10.1016/j.compositesb.2019.107618>.
- [51] Phase Equilibria Diagrams Online Database (NIST Standard Reference Database 31), The American Ceramic Society and the National Institute of Standards and Technology, 2021. Figure Numbers 5232, 93-023, 9327; www.nist.gov/srd/nist31.cfm, (n.d.).
- [52] S. Mungiguerra, G.D. [Di Martino], A. Cecere, R. Savino, L. Zoli, L. Silvestroni, D. Sciti, Ultra-high-temperature testing of sintered ZrB₂-based ceramic composites in atmospheric re-entry environment, *Int. J. Heat Mass Transf.* 156 (2020) 119910. doi:<https://doi.org/10.1016/j.ijheatmasstransfer.2020.119910>.
- [53] S. Mungiguerra, G.D. Di Martino, R. Savino, L. Zoli, L. Silvestroni, D. Sciti, Characterization of novel ceramic composites for rocket nozzles in high-temperature harsh environments, *Int. J. Heat Mass Transf.* 163 (2020) 120492. doi:<https://doi.org/10.1016/j.ijheatmasstransfer.2020.120492>.